Nanoscale

ROYAL SOCIETY OF CHEMISTRY

PAPER

View Article Online
View Journal | View Issue

Cite this: *Nanoscale*, 2025, **17**, 23387

Shape effects on the 2D self-assembly of lithographically fabricated nanoparticles

Yi-Yu Cai, †[a,b] Zeyu Gu,†[a] Shengsong Yang,[c] Christopher B. Murray[c,d] and Cherie R. Kagan *[a,c,d]

Received 12th August 2025,
Accepted 19th September 2025

DOI: 10.1039/d5nr03413b

rsc.li/nanoscale

We fabricate and polymer ligate square, pentagonal, and hexagonal nanoplates and investigate the effect of nanoparticle (NP) shape on the self-organization of their dispersions at a liquid–air interface into two-dimensional assemblies. Hexagonal NPs assemble into interlocking hexagonal lattices, exhibiting the highest translational order with a characteristic correlation length ($\xi_{0.5}$) extending over nine NP building blocks. Square NP assemblies are disordered, characterized by $\xi_{0.5}$ averaging around three NP units, consistent with the propensity of NPs to slide and form coexisting Λ_1 and Λ_0 lattices. Pentagonal NP assemblies show six-fold coordination, but do not fully tessellate the plane, yielding anisotropic assemblies with intermediate order and $\xi_{0.5}$ of about seven NP units. In binary NP assemblies, mixed pentagonal and hexagonal NP assemblies with shared six-fold coordination show greater ordering in comparison to assemblies of square and hexagonal NPs.

Introduction

The shape of nanoparticles (NPs), analogous to atomic valency, directs the order and motifs of self-assembled structures.[1–3] Geometrically, NP shape significantly impacts the thermodynamically favorable arrangement for dense packing.[4] Polygons with fewer than seven vertices, interacting primarily through steric hindrance, show a preference for edge-to-edge alignment,[5] due to shape-induced directional entropic forces generating more free volume.[6–8] Studies on the formation of two-dimensional structures or ordered lattices of polygons have employed both computational simulations and experimental methods at various length scales.[9–12] Regular hexagonal-shaped particles typically form a close-packed hexagonal lattice across nano-,[13,14] micro-,[15] and millimeter scales,[16] mirroring their intrinsic six-fold symmetry. The interlocking geometry of their superlattice results in a rigid structure that enhances translational order.[12] Square assemblies display more intrinsic disorder because they can slide along columns and rows, allowing for greater flexibility. The degree of corner rounding affects the packing density, as sharp corners result in a perfect square lattice,[9] while rounded corners lead to Λ_1 and Λ_0 lattice structures.[17] Experimental research has demonstrated the assembly of square particles into two-dimensional planes at both the nano[14] and micrometer scales,[18–20] showcasing diverse lattice structures. Unlike squares and hexagons, a regular pentagon cannot fully tessellate a plane.

The study of pentagonal NP assemblies spans multiple scales.[10] At the millimeter scale, pentagonal styrene particles subjected to hard-core interactions and weak hydrodynamic interactions on air tables exhibit ice-ray packing,[21] the densest known local configuration characterized by alternating stripes of particles in two distinct orientations.[22] Lithographically-defined microscale epoxy-based polymer particles assembled in aqueous environments form hexagonal rotator crystal structures, dominated by "hard" short-range repulsive in-plane interactions.[19,23,24] Translational and rotational jamming prevent the formation of ice-ray packing. At the nanometer scale, shape customization has originated largely from advances in chemical synthesis techniques, where achieving high uniformity in size and shape is a critical factor for the self-assembly of superlattices.[25,26] Colloidal penta-twinned elongated nanoprisms with pentagonal cross-sections self-assemble from dispersions into multilayered structures that adopt configurations ranging from dense ice-ray packing to less dense Dürer packing.[22] Chemical routes to synthesize nanoscale pentagonal plates are rare.[27] Thus, to our knowledge, there are few studies on the two-dimensional assembly of nanoscale pentagonal particles. Studies on the assembly of

[a]*Department of Electrical and Systems Engineering, University of Pennsylvania, Philadelphia, PA 19104, USA*
[b]*Macao Institute of Materials Science and Engineering (MIMSE), Faculty of Innovation Engineering, Macau University of Science and Technology, Taipa, Macao, 999078 China*
[c]*Department of Chemistry, University of Pennsylvania, Philadelphia, PA 19104, USA*
[d]*Department of Materials Science and Engineering, University of Pennsylvania, Philadelphia, PA 19104, USA. E-mail: kagan@seas.upenn.edu*
†These authors contributed equally.

pentagonal-shaped molecules have also been conducted. The interactions that govern their assembly diverge significantly from those in particle assemblies, falling outside the scope of this paper.[28]

In this study, we use nanoimprint lithography and thermal evaporation to fabricate Au nanoplates with precise control over size and shape, including square, pentagonal, and hexagonal geometries with identical side lengths, as a model system for studying two-dimensional self-assembly. These nanoplates are assembled into 2D extended monolayers *via* the liquid–air interface assembly technique.[29] Our quantitative analysis reveals that the translational order of the Au nanoplates follows the trend: hexagonal > pentagonal > square shape, attributed to shape symmetry, interlocking capability based on coordination number, and tiling ability. Furthermore, binary mixtures of pentagonal and hexagonal NPs, which exhibit a common six-fold coordination, yield greater translational order than their combinations with squares, demonstrating the influence of shape on self-assembly.

Results and discussion

The square, pentagonal, and hexagonal Au NPs are produced *via* a combination of nanoimprint lithography and thermal evaporation techniques (Fig. 1), as detailed in our previous work.[30] Briefly, e-beam lithography is employed to create imprint templates with the desired polygonal shapes. Here, templates are designed to produce NPs with uniform side lengths of approximately 220 nm. Wafers are coated with resist trilayers, and the shapes are transferred into the top thermal Nanonex resist layer and middle polydimethylglutarimide (PMGI) undercut layer through imprinting and developing. Subsequently, a layer of Au or other materials is physically evaporated onto the patterned resist layers, and upon liftoff, yields the NPs anchored by the bottom sacrificial Durimide layer. To ensure the dispersion of the NPs in solvents, the Au NPs are coated with a thiolated-polystyrene polymer (number-average molecular weight M_n = 50k) in a tetrahydrofuran (THF) solution. The coated NPs are then harvested from the wafer by immersion and sonication in *N*-methyl-2-pyrrolidone (NMP). Through a series of centrifugation and redispersion steps in organic solvents, we remove excess polymer ligands and concentrate approximately 10^8 NPs into less than 5 μL of a mixed organic solvent of either chloroform and toluene or THF and toluene, with a volume ratio of 1 : 3. Transmission electron microscopy (TEM) images show that the NPs have a uniform polymer coating of approximately 7 ± 1 nm in thickness (Fig. S1). Thiol-terminated polystyrene ligands on Au nanoplates provide short-range steric stabilization in our assembly solvents; given the thin polymer shell relative to plate size, packing is shape-dominated rather than ligand-directed, consistent with prior studies of self-assembly and polymer-grafted nanoparticles.[31–33]

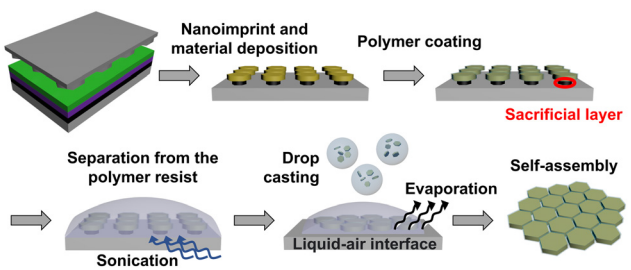

Fig. 1 Schematic of the preparation and self-assembly of polygonal NP dispersions. Square, pentagonal, and hexagonal Au NPs are fabricated *via* nanoimprint lithography and thermal evaporation of thin films. After liftoff of the resist, NPs remain bound to the wafer. These NPs are subsequently coated with a thiolated polystyrene polymer layer, facilitating their harvesting through sonication and stable dispersion in liftoff solvents. The self-assembly process is carried out at a liquid–air interface, with NPs dispersed in a hydrophobic phase (toluene, tetrahydrofuran, chloroform) atop a hydrophilic ethylene glycol layer. As the ethylene glycol evaporates, assembled NP layers are deposited on the underlying wafers.

The Au NP dispersions are then dropped onto an ethylene glycol subphase, forming distinct hydrophobic organic phases. As the organic solvent evaporates, NP films emerge on the surface of the ethylene glycol. Wafers are submerged in the ethylene glycol subphase, and the ethylene glycol is evaporated through vacuum drying, depositing NP films on the wafers. NP assemblies are subsequently imaged in the SEM, and the images are analyzed to quantify their structure, including the shapes, positions, orientations, and long-range order of the NPs. The analysis techniques applied to all images include Fourier transforms (FFTs), 2D nearest-neighbor positional distributions, 2D autocorrelation functions, and full pair position probability distributions, allowing for comprehensive characterization of the assembled structures.[12] Detailed orientational maps and lattice-type classifications are provided in Fig. S2.

Fig. 2 shows the distinct structures for square, pentagonal, and hexagonal Au NP assemblies. Hexagonal Au NP assemblies form highly uniform (Fig. 2C(I)), close-packed hexagonal lattice structures, as depicted in Fig. 2C(I) inset.[14] Uniform particle alignment is evidenced by consistent coloration across the image in Fig. S2C, where colors represent particle orientation angles, as well as by the sharp peaks in FFTs (Fig. 2C (II)). 2D nearest-neighbor positional distributions (Fig. 2C(III)) quantify the likelihood of locating a neighboring NP at a specific distance.[12] They reveal a nearly isotropic spread in distance with a major-to-minor axis FWHM ratio of 1.09 ± 0.07, the closest to unity among all shapes studied. Square Au NP assemblies exhibit the coexistence of Λ_0 and Λ_1 lattices (Fig. 2A and S2A). In the Λ_0 lattice, square NPs align in rows with their faces offset by half a side length, shown in blue in the inset of Fig. 2A(I). In contrast, the Λ_1 lattice, colored pink in the same inset, is characterized by squares with rounded corners that touch, forming a rhombic symmetry.[18] The lattice-type detection and orientational analysis used to distinguish Λ_0 from Λ_1 are illustrated in Fig. S2A. The 2D FFTs of the images for square Au NP assemblies show discernible peaks (Fig. 2A(II)), though less pronounced compared to those for other NP shapes, reflecting the disorder from the coexistence of mul-

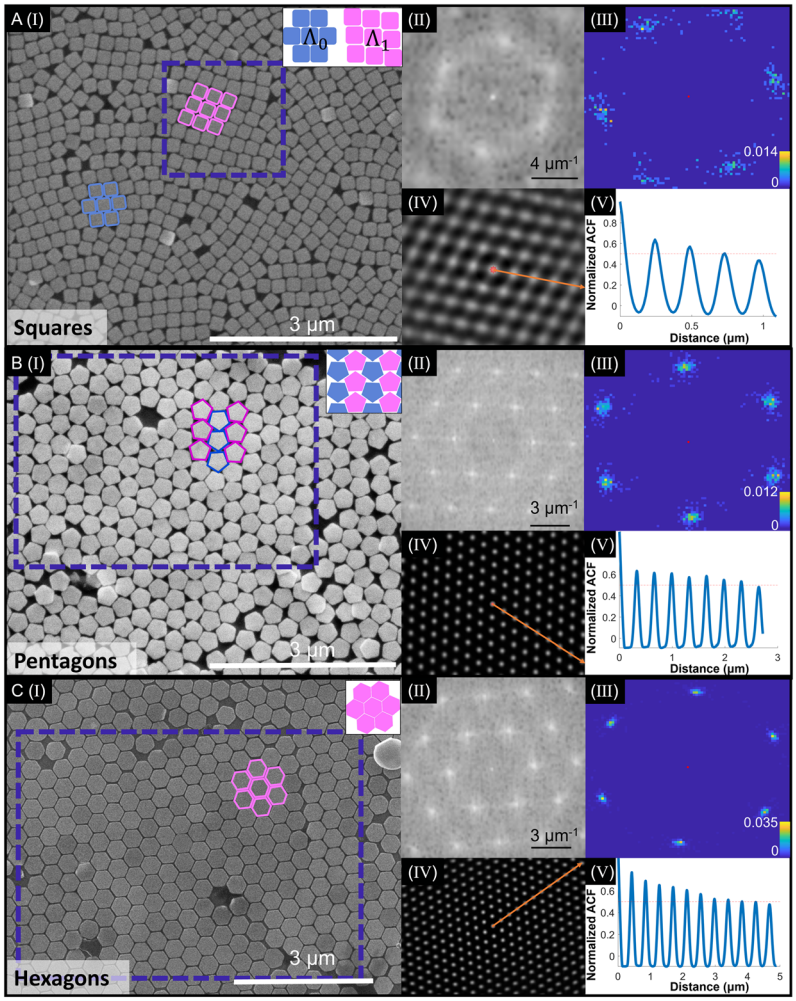

Fig. 2 Structural analysis of (A) square, (B) pentagonal, and (C) hexagonal Au NP assemblies. Each set includes: (I) SEM images, regions with colored outlines and insets showing representative lattices, (II) FFTs of SEM images, (III) 2D probability distributions of nearest-neighbor positional patterns, (IV) 2D autocorrelation functions, and (V) linecut profiles from the 2D autocorrelation in the marked regions.

tiple lattices (Fig. 2A(II)). The 2D nearest-neighbor positional distributions (Fig. 2A(III)) of square NPs show the highest anisotropy with a major-to-minor axis FWHM ratio of 2.39 ± 0.29, indicating strong directional differences in the translational correlations.

Pentagonal Au NP assemblies exhibit ice-ray packing with antiparallel arrangements indicated by alternating purple and blue colors in Fig. 2B and Fig. S2B.[22] Other areas form a hexagonal rotator crystal phase,[23] maintaining positional order but lacking consistent orientational order. FFTs of pentagonal Au NP assemblies reveal a hexagonal pattern (Fig. 2B(II)), consistent with distinct peaks in 2D nearest-neighbor positional distributions (Fig. 2B(III)). Quantitative analysis of 2D nearest-neighbor positional distributions shows an intermediate level of anisotropy (major-to-minor axis FWHM ratio of 1.80 ± 0.12) between hexagonal and square assemblies. However, the expected rectangular symmetry of antiparallel-patterned ice-ray packing is absent in the FFTs, likely due to local variations and imperfections in the antiparallel structure observed in the image.[34]

To quantitatively compare the long-range positional order across different NP shapes, we utilized 2D autocorrelation functions derived from SEM images (Fig. 2A–C(iv)). These functions measure the self-similarity of the image as the displacement vector changes. The $\xi_{0.5}$ value of translational order is defined at points where the oscillation in the line profiles drops to less than 50% of their initial value (Fig. 2A–C(v)). To determine the $\xi_{0.5}$ value for each polygonal NP assembly, we start with a well-ordered region in each SEM image to measure $\xi_{0.5}$. As the area expands, the $\xi_{0.5}$ value typically reaches a maximum before decreasing due to the inclusion of less ordered regions. This approach enables us to identify the maximum analysis area for each shape, capturing the best-case scenario for order without being constrained by a fixed area across different shapes, as exemplified by the selected areas shown in Fig. 2A–C(V). Using this method, we observe that hexagonal NPs exhibit a maximal $\xi_{0.5}$ value of 9.2 ± 0.8 repeating units (Table S1), in contrast to 6.8 ± 0.4 for pentagonal Au NPs. Square Au NPs show a lower maximal $\xi_{0.5}$ value of

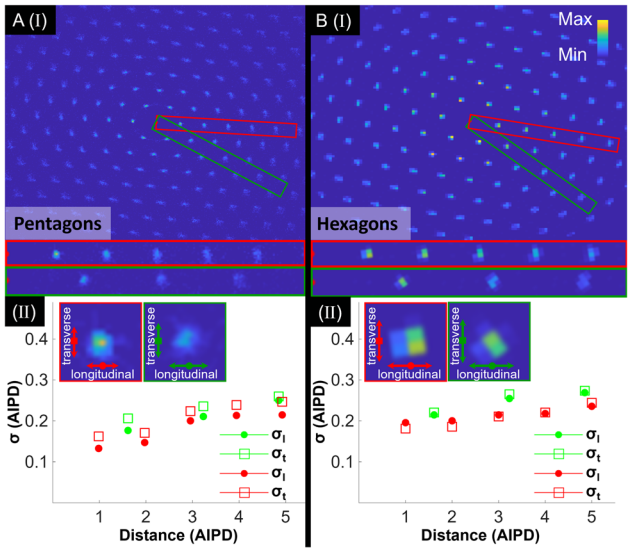

Fig. 3 Analysis of the 2D pair position distribution function for (A) pentagonal and (B) hexagonal Au NP assemblies. Each set includes: (I) 2D pair position probability distributions with corresponding linecuts in the [11$\bar{2}$0] (red) and [1$\bar{1}$00] (green) directions. (II) Insets: definitions of the width of the position probability distribution for the first peak away from the center. Peak widths, in units of average interparticle distance (AIPD), for the [11$\bar{2}$0] (red) and [1$\bar{1}$00] (green) directions in both longitudinal and transverse orientations are plotted against interparticle distance.

3.2 ± 0.4, likely due to the presence of multiple lattices and their propensity to slide.

The translational order in pentagonal and hexagonal Au NP assemblies is further analyzed through the full pair position probability distribution,[35] which assesses the likelihood of locating an NP at a specific location, given that another NP is positioned at the origin (Fig. 3). A broader peak in this distribution indicates increased disorder, reflecting a similar accumulation of lattice disorder in both pentagonal and hexagonal Au NP assemblies across various lattice directions, and in longitudinal (σ_l) and transverse (σ_t) orientations. However, the key distinction is that well-ordered hexagonal Au NP assemblies exhibit isotropic translational order, with σ_l roughly equal to σ_t. In contrast, pentagonal Au NP assemblies consistently show anisotropic translational order, with σ_l smaller than σ_t, revealing a dominance of shearing over compressive or tensile disorder. The anisotropy in pentagonal Au NP assemblies is attributed to their inability to tessellate a plane without creating voids, thereby facilitating the sliding of rows or columns. While this allows for more flexibility than for hexagonal NP assembly, pentagonal NPs still achieve a higher degree of order than square NPs as their six-fold coordination partially restricts NP translation. While lateral capillary forces from contact-line distortions may contribute to particle interactions at short range,[36] the trends observed in systematic shape-dependent assembly are consistent with geometric constraints and entropic forces dominating the assembly process for these sub-micron particles.[4,29]

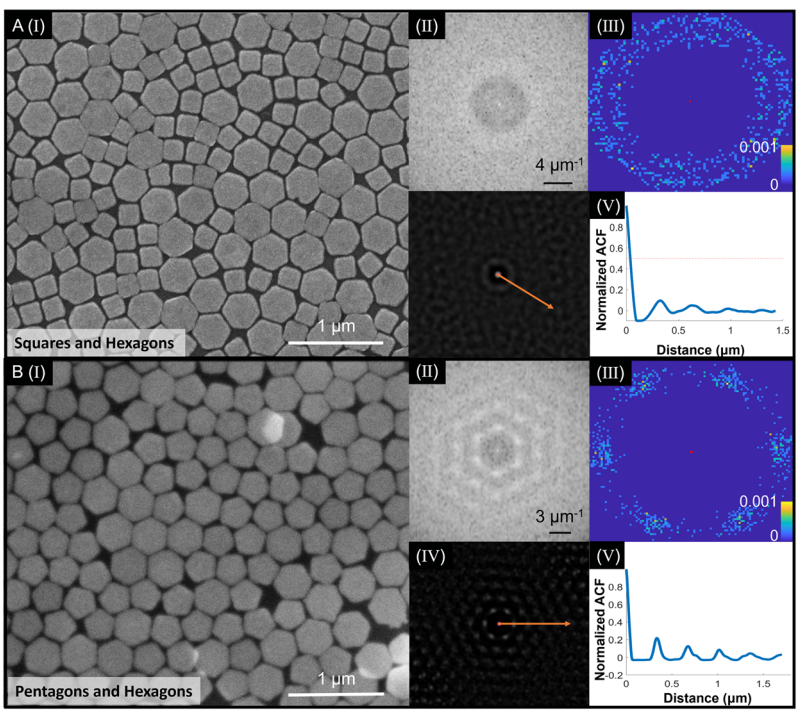

Fig. 4 Structural analysis of (A) square–hexagonal and (B) pentagonal–hexagonal Au NP assemblies. Each set includes: (I) SEM images and their (II) FFTs, (III) 2D probability distributions of nearest-neighbor positional patterns, (IV) 2D autocorrelation functions, and (V) linecut profiles from the 2D autocorrelation.

We mix combinations of the polygonal Au NPs to form binary mixtures, specifically pentagonal–hexagonal and square–hexagonal combinations (Fig. 4). Both binary mixtures exhibit a degree of phase separation, where particles of the same shape tend to cluster together, as visible in the SEM images (Fig. 4A and B(I)). The pentagonal–hexagonal mixture has sharper and more distinct peaks in the FFTs (Fig. 4A and B(II)), indicating better long-range order. The 2D nearest-neighbor position distributions reveal a clearer hexagonal pattern for the pentagonal–hexagonal mixture (Fig. 4B(III)). In contrast, the square–hexagon mixture shows a dual-ring structure without distinct peaks (Fig. 4A(III)), reflecting different nearest-neighbor distances for different shapes and a less uniform local structure. The autocorrelation analysis (Fig. 4A and B(IV)) and the line profiles for both mixtures (Fig. 4A and B(V)) show peak heights below 0.5, indicating limited coherence. The pentagonal–hexagonal mixture displays more pronounced and regularly spaced peaks compared to the square–hexagon mixture, indicating higher translational order and longer-range correlations. The split peaks observed in the pentagonal–hexagonal autocorrelation likely arise from the coexistence of multiple characteristic distances between particles of both identical and differing shapes in the binary system. This improved ordering in the pentagonal–hexagonal system benefits from their geometric compatibility, both having six nearest neighbors. The lower order in the square–hexagonal mixture[11] is likely due to the incompatibility between the different lattice structures as squares can form both Λ_0 and Λ_1 lattices and hexagons pack in a hexagonal lattice.

Conclusions

In this study, we explore how polygonal shape influences the 2D self-assembly of lithographically fabricated nanoplates, with a focus on square, pentagonal, and hexagonal NPs. Analysis of translational order reveals a clear hierarchy: hexagonal NPs form the most ordered assemblies due to their interlocking hexagonal lattices, square NPs exhibit the most disorder with coexisting Λ_1 and Λ_0 lattices, while pentagonal NPs show intermediate, anisotropic order. This behavior stems from the geometries of each shape and their ability to tile a plane. Similar shape-driven hierarchies of translational order have been directly observed for colloidal nanocrystals at the tens-of-nanometer scale, where van der Waals and ligand-mediated interactions dominate. In this regime, ligand length/coverage sets the interparticle gap and effectively rounds particle corners, thereby modulating directional entropic forces and, in turn, translational coherence.[4,12] Beyond the assembly of a single shape, we show that binary mixtures of pentagonal and hexagonal NPs achieve higher translational order through shared coordination numbers, in contrast to the comparatively disordered square–hexagon mixtures. To our knowledge, this provides nanoscale experimental evidence that coordination compatibility can mitigate demixing and enhance order in a binary polygonal system (pentagon–hexagon); by contrast, prior simulations of other symmetric polygon mixtures (*e.g.*, hexagon–square/triangle) predict demixing unless shape- or edge-specific patches are introduced.[11]

Our approach to NP fabrication and assembly was also applied to create 2D extended assemblies of binary mixtures of hexagonal Au and Ag NPs, as well as hexagonal Ge NPs, suggesting its broad applicability (Fig. S3). This research opens avenues for further exploration into the self-assembly of NPs with anisotropic, complex shapes (such as convex and concave polygons), varied sizes, and compositions with entropic and enthalpic patchy interactions.[11,37–39] By integrating NPs of various types, we plan to design functional materials that leverage the combined properties of the constituent particles for applications in optics and opto-electronics. For example, close-packed monolayers of hexagonal nanoplates provide uniform nearest-neighbor gaps and edge sites that yield reproducible near-field hot spots and enable quantitative SERS.[40,41] Our previous work showed that symmetry and interparticle gaps in polygonal NP metamolecules tune the Fano lineshapes and polarization response,[30] and correlated single-domain spectroscopy on binary nanocrystal superlattices further demonstrates that lattice symmetry and composition systematically control near-field coupling and resonance energy.[42] For electronic/optoelectronic devices, edge-to-edge assembly of cubic-shaped quantum dots with short interparticle spacings enhances coupling and charge transport in quantum-dot assemblies, compared to those composed of spherical quantum dots.[43,44]

Conflicts of interest

There are no conflicts to declare.

Data availability

The data supporting this article have been included as part of the supplementary information (SI). The data that support the findings of this study are available from the corresponding author upon reasonable request. Supplementary information is available. See DOI: **https://doi.org/10.1039/d5nr03413b**.

Acknowledgements

The authors gratefully thank the Office of Naval Research Multidisciplinary University Research Initiative Award ONR N00014-18-1-2497 for primary support of the work, including NP nanofabrication, assembly, and characterization. Y. C. acknowledges the Science and Technology Development Fund (FDCT), Macao SAR (Grant No. 0024/2024/RIB1, 0136/2024/RIA2) and the National Natural Science Foundation of China (Grant No. 12404421) for support during the writing of this manuscript. The nanofabrication was conducted partially at the Singh Center for Nanotechnology, which was supported by the NSF National Nanotechnology Coordinated Infrastructure Program under grant NNCI-2025608. This research also uti-

lized the electron beam lithography infrastructure at the Center for Functional Nanomaterials (CFN), a U.S. Department of Energy Office of Science User Facility located at Brookhaven National Laboratory, under Contract No. DE-SC0012704.

References

1 J. Gong, R. S. Newman, M. Engel, M. Zhao, F. Bian, S. C. Glotzer and Z. Tang, *Nat. Commun.*, 2017, **8**, 14038.
2 S. C. Glotzer and M. J. Solomon, *Nat. Mater.*, 2007, **6**, 557–562.
3 G. van Anders, N. K. Ahmed, R. Smith, M. Engel and S. C. Glotzer, *ACS Nano*, 2014, **8**, 931–940.
4 M. A. Boles, M. Engel and D. V. Talapin, *Chem. Rev.*, 2016, **116**, 11220–11289.
5 J. A. Anderson, J. Antonaglia, J. A. Millan, M. Engel and S. C. Glotzer, *Phys. Rev. X*, 2017, **7**, 021001.
6 G. van Anders, D. Klotsa, N. K. Ahmed, M. Engel and S. C. Glotzer, *Proc. Natl. Acad. Sci. U. S. A.*, 2014, **111**, E4812–E4821.
7 E. S. Harper, G. van Anders and S. C. Glotzer, *Proc. Natl. Acad. Sci. U. S. A.*, 2019, **116**, 16703–16710.
8 T. Vo and S. C. Glotzer, *Proc. Natl. Acad. Sci. U. S. A.*, 2022, **119**, e2116414119.
9 C. Avendaño and F. A. Escobedo, *Soft Matter*, 2012, **8**, 4675–4681.
10 T. Schilling, S. Pronk, B. Mulder and D. Frenkel, *Phys. Rev. E*, 2005, **71**, 036138.
11 J. A. Millan, D. Ortiz, G. van Anders and S. C. Glotzer, *ACS Nano*, 2014, **8**, 2918–2928.
12 J. C. Ondry, L. B. Frechette, P. L. Geissler and A. P. Alivisatos, *Nano Lett.*, 2022, **22**, 389–395.
13 F. Qin, X. Cui, Q. Ruan, Y. Lai, J. Wang, H. Ma and H.-Q. Lin, *Nanoscale*, 2016, **8**, 17645–17657.
14 X. Ye, J. E. Collins, Y. Kang, J. Chen, D. T. N. Chen, A. G. Yodh and C. B. Murray, *Proc. Natl. Acad. Sci. U. S. A.*, 2010, **107**, 22430–22435.
15 T. D. Clark, J. Tien, D. C. Duffy, K. E. Paul and G. M. Whitesides, *J. Am. Chem. Soc.*, 2001, **123**, 7677–7682.
16 N. Bowden, I. S. Choi, B. A. Grzybowski and G. M. Whitesides, *J. Am. Chem. Soc.*, 1999, **121**, 5373–5391.
17 Y. Jiao, F. H. Stillinger and S. Torquato, *Phys. Rev. Lett.*, 2008, **100**, 245504.
18 J.-M. Meijer, V. Meester, F. Hagemans, H. N. W. Lekkerkerker, A. P. Philipse and A. V. Petukhov, *Langmuir*, 2019, **35**, 4946–4955.
19 K. Zhao, R. Bruinsma and T. G. Mason, *Proc. Natl. Acad. Sci. U. S. A.*, 2011, **108**, 2684–2687.
20 L. Rossi, V. Soni, D. J. Ashton, D. J. Pine, A. P. Philipse, P. M. Chaikin, M. Dijkstra, S. Sacanna and W. T. M. Irvine, *Proc. Natl. Acad. Sci. U. S. A.*, 2015, **112**, 5286–5290.
21 Y. L. Duparcmeur, A. Gervois and J. P. Troadec, *J. Phys.: Condens. Matter*, 1995, **7**, 3421.
22 J. Marcone, W. Chaâbani, C. Goldmann, M. Impéror-Clerc, D. Constantin and C. Hamon, *Nano Lett.*, 2023, **23**, 1337–1342.
23 K. Zhao and T. G. Mason, *Phys. Rev. Lett.*, 2009, **103**, 208302.
24 P.-Y. Wang and T. G. Mason, *Nature*, 2018, **561**, 94–99.
25 C. B. Murray, C. R. Kagan and M. G. Bawendi, *Annu. Rev. Mater. Sci.*, 2000, **30**, 545–610.
26 C. B. Murray, C. R. Kagan and M. G. Bawendi, *Science*, 1995, **270**, 1335–1338.
27 J. J. Velázquez-Salazar, L. Bazán-Díaz, Q. Zhang, R. Mendoza-Cruz, L. Montaño-Priede, G. Guisbiers, N. Large, S. Link and M. José-Yacamán, *ACS Nano*, 2019, **13**, 10113–10128.
28 C. Yuan, N. Xue, X. Zhang, Y. Zhang, N. Li, Q. Xue, T. Wu, S. Hou and Y. Wang, *Chem. Commun.*, 2019, **55**, 5427–5430.
29 A. Dong, J. Chen, P. M. Vora, J. M. Kikkawa and C. B. Murray, *Nature*, 2010, **466**, 474–477.
30 Y.-Y. Cai, A. Fallah, S. Yang, Y. C. Choi, J. Xu, A. Stein, J. M. Kikkawa, C. B. Murray, N. Engheta and C. R. Kagan, *Adv. Mater.*, 2023, **35**, 2301323.
31 J. C. Conrad and M. L. Robertson, *JACS Au*, 2023, **3**, 333–343.
32 J. W. Yu, H. Yun, W. B. Lee and Y. Kim, *Adv. Sci.*, 2024, **11**, 2406720.
33 M. A. Boles and D. V. Talapin, *J. Am. Chem. Soc.*, 2015, **137**, 4494–4502.
34 S. Pichler, M. I. Bodnarchuk, M. V. Kovalenko, M. Yarema, G. Springholz, D. V. Talapin and W. Heiss, *ACS Nano*, 2011, **5**, 1703–1712.
35 B. H. Savitzky, R. Hovden, K. Whitham, J. Yang, F. Wise, T. Hanrath and L. F. Kourkoutis, *Nano Lett.*, 2016, **16**, 5714–5718.
36 P. A. Kralchevsky, N. D. Denkov and K. D. Danov, *Langmuir*, 2001, **17**, 7694–7705.
37 N. Pakalidou, J. Mu, A. J. Masters and C. Avendaño, *Mol. Syst. Des. Eng.*, 2020, **5**, 376–384.
38 J. A. Millan, D. Ortiz and S. C. Glotzer, *Soft Matter*, 2015, **11**, 1386–1396.
39 E. S. Harper, R. L. Marson, J. A. Anderson, G. van Anders and S. C. Glotzer, *Soft Matter*, 2015, **11**, 7250–7256.
40 L. Xing, Y. Xiahou, X. Zhang, W. Du, P. Zhang and H. Xia, *ACS Appl. Mater. Interfaces*, 2022, **14**, 13480–13489.
41 S. Simitha, D. Mohan, S. Regi, J. Jacob and V. Ipe Thomas, *Mater. Today: Proc.*, 2023, **93**, 66–72.
42 X. Ye, J. Chen, B. T. Diroll and C. B. Murray, *Nano Lett.*, 2013, **13**, 1291–1297.
43 W.-K. Koh, S. R. Saudari, A. T. Fafarman, C. R. Kagan and C. B. Murray, *Nano Lett.*, 2011, **11**, 4764–4767.
44 P. Liljeroth, K. Overgaag, A. Urbieta, B. Grandidier, S. G. Hickey and D. Vanmaekelbergh, *Phys. Rev. Lett.*, 2006, **97**, 096803.

